High-Fidelity CFD Investigation of the Aerodynamic Influence of Fairing Integration for Helicopter Electrification Systems

Octavian-Mircea CRISAN[1], Alexandru PASULA[1], Ionut BUNESCU[2,3], Mihai-Vladut HOTHAZIE[2,3], Mihai-Victor PRICOP*[,2,3], Bogdan RUSU[2], Dumitru PEPELEA[2], Mihaita-Gilbert STOICAN[2,3]

*Corresponding author
[1]ATNOM SRL,
Bicazului Street No. 6-8 Oradea
[2]INCAS – National Institute for Aerospace Research "Elie Carafoli",
B-dul Iuliu Maniu 220, Bucharest 061126, Romania
[3]National University of Science and Technology POLITEHNICA,
Splaiul Independentei nr. 313, Sector 6, Cod Poștal 060042, Bucharest, Romania,
pricop.victor@incas.ro*

DOI: 10.13111/2066-8201.2026.18.2.2

Received: 07 May 2026/ Accepted: 25 May 2026/ Published: June 2026

Abstract: *The electrification of rotary-wing aircraft introduces new aerodynamic challenges associated with the integration of batteries, electric propulsion systems, and thermal management components within the helicopter fuselage. This study investigates the aerodynamic influence of an external fairing designed to accommodate the electrification architecture of a light helicopter using high-fidelity Computational Fluid Dynamics (CFD) simulations. Two configurations were analyzed: the baseline helicopter geometry and the modified configuration incorporating an aerodynamic fairing enclosing the electric motor, battery modules, and cooling system. Three-dimensional numerical simulations were performed using Ansys Fluent on high-quality unstructured meshes generated in Fluent Meshing. The simulations considered multiple forward-flight velocities and altitude conditions in order to evaluate the aerodynamic behavior over a broad operational envelope. The numerical setup employed the Reynolds-Averaged Navier–Stokes (RANS) equations coupled with turbulence modeling to capture flow separation, wake development, and interaction effects between the fuselage, fairing, and rotor-induced flow structures. Results indicate that the integration of the aerodynamic fairing significantly improves the flow uniformity around the electrification components while reducing adverse flow recirculation regions. Furthermore, the modified configuration demonstrates improved aerodynamic efficiency at medium and high forward-flight velocities, with noticeable reductions in drag penalties compared to the non-faired electrification layout. Velocity field visualizations and streamline analyses reveal smoother flow attachment and reduced wake intensity around the fuselage–tail boom junction. The study highlights the importance of aerodynamic optimization in electric helicopter integration and demonstrates the capability of high-fidelity CFD methodologies for evaluating advanced electrified rotorcraft configurations.*

Key Words: *light helicopter, electric power, podded accumulator, CFD, flight performance, actuating disk.*

1. INTRODUCTION

The global aerospace industry is currently experiencing a major technological transition driven by the necessity to reduce greenhouse gas emissions, operational costs, and environmental impact. Within this context, aircraft electrification has emerged as one of the most promising research directions for future aviation systems. Electrified propulsion architectures, including fully electric and hybrid-electric concepts, are being actively investigated for both fixed-wing and rotary-wing aircraft due to their potential to improve energy efficiency, reduce acoustic emissions, and decrease dependence on fossil fuels [1–3].

While substantial progress has been achieved in the electrification of fixed-wing aircraft, the electrification of rotary-wing platforms remains significantly more challenging. Helicopters operate under highly complex aerodynamic conditions involving strong rotor-induced flows, wake interactions, vortex structures, and unsteady aerodynamic phenomena. In addition, rotary-wing aircraft require high power-to-weight ratios and efficient thermal management systems, making the integration of electric propulsion components particularly difficult [4, 5]. One of the primary challenges associated with helicopter electrification is the physical integration of batteries, electric motors, power electronics, and cooling systems into existing airframes. Unlike conventional turbine-powered helicopters, electric propulsion systems require large-volume battery modules and dedicated cooling architectures, which may significantly alter the external geometry of the aircraft. These geometric modifications can generate additional aerodynamic drag, increase flow separation regions, and negatively affect the global aerodynamic efficiency of the helicopter [6].

To minimize these aerodynamic penalties, external aerodynamic fairings are frequently employed in aerospace engineering. In conventional aviation applications, aerodynamic fairings are commonly used for landing gear systems, external fuel tanks, sensor housings, and fuselage–wing junctions [7]. Their application in electric rotorcraft integration represents a relatively new and rapidly developing research area. Recent advances in Computational Fluid Dynamics (CFD) have enabled the detailed numerical investigation of complex rotorcraft aerodynamic phenomena. High-fidelity CFD methods are now extensively used to study rotor–fuselage interactions, wake development, vortex dynamics, and aerodynamic optimization of helicopter configurations [8–10]. Modern CFD approaches based on Reynolds-Averaged Navier–Stokes (RANS), Detached Eddy Simulation (DES), and Large Eddy Simulation (LES) provide accurate predictions of separated turbulent flows around highly complex three-dimensional geometries. Several studies have focused on the aerodynamic optimization of helicopter fuselages and drag reduction strategies. Johnson [11] investigated the aerodynamic efficiency of advanced rotorcraft configurations and highlighted the importance of minimizing fuselage drag in improving overall vehicle performance. Le Pape and Costes [12] analyzed helicopter fuselage aerodynamics using numerical simulations and demonstrated the strong influence of local geometry modifications on wake topology and pressure distribution.

In the context of electric aircraft integration, aerodynamic challenges become even more significant because battery systems and thermal management components frequently require additional external volumes. Thermal management systems are particularly important in electric propulsion architectures because batteries and electric motors generate considerable heat during operation. Consequently, dedicated cooling ducts and air intakes are often necessary, potentially introducing additional aerodynamic disturbances [13].

The aerodynamic interaction between external housings and the surrounding flow field may lead to increased parasitic drag, premature flow separation, wake asymmetry, enhanced turbulence intensity, reduced flight efficiency. Therefore, the aerodynamic optimization of

electrification integration structures is essential for maintaining acceptable rotorcraft performance. Recent research in electric vertical take-off and landing (eVTOL) aircraft has shown that aerodynamic shaping and fairing optimization can substantially improve energy efficiency and flight endurance [14]. Although eVTOL configurations differ from conventional helicopters, many aerodynamic integration challenges are similar, particularly regarding distributed electric propulsion systems and cooling architecture placement.

Despite the growing interest in electric rotorcraft technologies, relatively few studies have specifically investigated the aerodynamic effects of integrating electrification fairings into helicopter fuselages using high-fidelity CFD approaches. Most existing works focus primarily on propulsion system design, battery technologies, or overall vehicle conceptual development, while detailed aerodynamic analyses of fairing integration remain limited [15]. The present work aims to address this research gap by performing a high-fidelity CFD investigation of a light helicopter equipped with an aerodynamic fairing designed to integrate electrification components. The study considers both the baseline helicopter geometry and a modified electrified configuration incorporating battery modules, electric propulsion components, cooling systems, external aerodynamic fairings. Three-dimensional numerical simulations are carried out using Ansys Fluent on high-quality unstructured meshes generated in Fluent Meshing. Multiple flight conditions and operational altitudes are investigated to evaluate the aerodynamic influence of the fairing over a broad flight envelope.

2. METHODOLOGY

For the numerical investigation, an initial generic helicopter geometry was developed based on realistic full-scale dimensions representative of a light rotorcraft configuration. The geometry includes the main fuselage, landing skids, tail and rotor. The baseline configuration was modified to integrate the electrification architecture, including the electric propulsion system, battery modules, and cooling system.

In order to accommodate the electrified propulsion architecture, an external aerodynamic fairing was introduced on the lateral region of the fuselage. The fairing was designed to ensure aerodynamic continuity between the fuselage and the newly integrated electrical components while minimizing flow disturbances and parasitic drag generation. A comparison between the two geometries is presented in Figure 1.

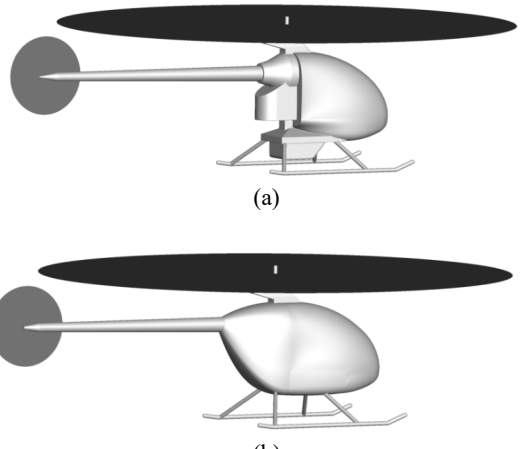

(a)

(b)

Figure 1. Comparison between (a) reference and (b) electrified geometry

The electrified configuration includes the electric propulsion motor, battery cell modules, cooling system and the external aerodynamic fairing. The fairing geometry was designed to provide a smooth aerodynamic transition between the helicopter fuselage and the electrification compartment.

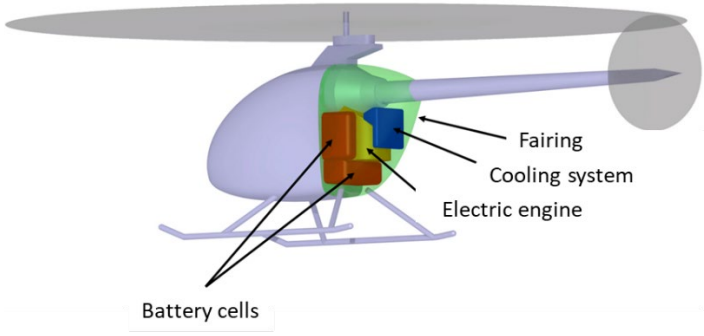

Figure 2. Aerodynamic fairing and electrified propulsion system architecture integration

The computational domain was defined using a spherical enclosure surrounding the helicopter geometry. The radius of the computational domain was set to 50 m, ensuring sufficient distance between the helicopter and the external boundaries of the numerical domain. The domain dimensions were selected based on preliminary sensitivity analyses and common CFD practices for external aerodynamic simulations involving rotorcraft configurations. The computational domain contains the helicopter fuselage, the aerodynamic fairing, the actuator disk associated with the main rotor and the actuator disk corresponding to the tail rotor.

The main and tail rotors were modeled using the actuator disk method implemented within Ansys Fluent. This approach allows the aerodynamic influence of the rotor systems to be represented without explicitly modeling the rotating blades, significantly reducing computational cost while preserving the global rotor-induced flow characteristics.

The computational grid was generated using the Fluent Meshing module available within the Ansys Workbench environment. Considering the geometric complexity of the helicopter configuration and the multiple aerodynamic interaction regions associated with the fuselage, fairing, landing skids, and rotor systems, an unstructured volumetric discretization strategy was adopted.

A curvature-based sizing function was employed to automatically refine the mesh in areas with reduced local curvature radius. The minimum surface element size was approximately $1\,mm$ while the maximum element size reached $3\,m$ in the far-field region of the computational domain. Smooth transition laws between neighboring refinement zones were applied to maintain acceptable mesh growth rates and ensure numerical stability.

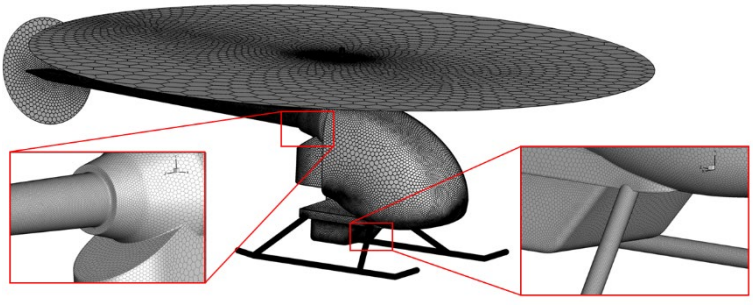

(a)

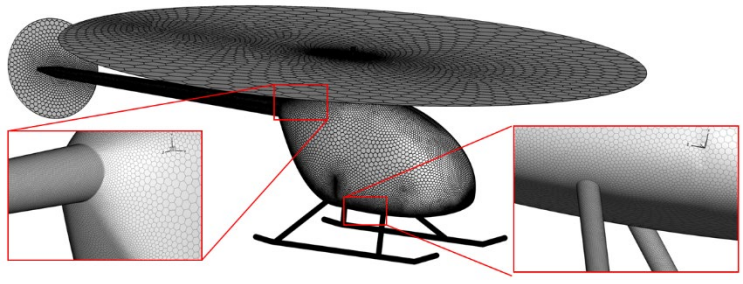

(b)

Figure 3. Representation of the surface mesh for (a) reference and (b) electrified geometry

In order to accurately resolve the boundary layer region, inflation layers were generated using prism-type elements extruded normal to the wall surfaces. A growth ratio of 1.1 and a first cell height that corresponds to a $y^+ = 1$ was employed to ensure smooth transition between the viscous sublayer region and the outer tetrahedral volume mesh and the use of the $k - \omega\ SST$ turbulence model.

Additional volumetric refinements were also introduced in regions where strong aerodynamic interactions were expected to occur. These regions include the actuator disk zones associated with the main rotor and tail rotor, the downstream wake development area, the fuselage–tail boom interaction region, and the wake generated by the aerodynamic fairing. The local refinement near the rotor actuator disks was necessary to accurately capture the rotor-induced velocity field and the associated momentum exchange generated by the actuator disk model. Similarly, the downstream wake region was refined in order to properly resolve the velocity deficit zones, wake diffusion mechanisms, and the evolution of the turbulent flow structures behind the helicopter configuration. Low skewness values and acceptable orthogonality levels were maintained across the computational domain to improve numerical robustness and reduce discretization errors. A mesh sensitivity analysis was additionally performed in order to verify that the numerical results were not strongly dependent on the discretization level. The adopted grid containing approximately 3.6 million polyhedral elements was found to represent an optimal compromise between numerical accuracy, computational cost. The numerical simulations were performed using Ansys Fluent. For the investigated flight conditions, the airflow was modeled as incompressible, steady-state, and inviscid. Atmospheric conditions corresponding to sea level were considered. The numerical model is based on the incompressible continuity and momentum conservation equations, coupled with the $k - \omega\ SST$ turbulence model:

$$\nabla \cdot \vec{V} = 0 \tag{1}$$

$$\rho(\vec{V} \cdot \nabla)\vec{V} = -\nabla p + \nabla \cdot \left[(\mu + \mu_t)\left(\nabla\vec{V} + \nabla\overrightarrow{V^T}\right)\right] + \overrightarrow{S_{ADM}} \tag{2}$$

$$\frac{\partial(\rho k)}{\partial t} + \frac{\partial(\rho k u_i)}{\partial x_i} = \frac{\partial}{\partial x_j}\left(\Gamma_k \frac{\partial k}{\partial x_j}\right) + G_k - Y_k + S_k \tag{3}$$

$$\frac{\partial(\rho\omega)}{\partial t} + \frac{\partial(\rho\omega u_i)}{\partial x_i} = \frac{\partial}{\partial x_j}\left(\Gamma_\omega \frac{\partial \omega}{\partial x_j}\right) + G_\omega - Y_\omega + D_\omega + S_\omega \tag{4}$$

where $\vec{V}$ is the velocity vector, u_i are the velocity components, ρ is the air density, p is the static pressure, μ is the dynamic viscosity, μ_t is the turbulent viscosity, k is the turbulent

kinetic energy, and ω is the specific dissipation rate. The term $\vec{S}_{ADM}$ represents the momentum source introduced by the actuator disk model for the main and tail rotors. G_k and G_ω are turbulence production terms, Y_k and Y_ω are dissipation terms, Γ_k and Γ_ω are effective diffusivities, and D_ω is the cross-diffusion term of the SST formulation.

The aerodynamic influence of the rotor systems was approximated using actuator disks implemented through fan-type boundary conditions. Virtual disk surfaces were positioned at the locations of the main and tail rotors, imposing pressure jumps equivalent to the rotor thrust generation. This approach enables the simulation of the rotor-induced velocity field and wake development without explicitly modeling the rotating blades, significantly reducing the computational cost while preserving the global rotor–fuselage aerodynamic interactions. A velocity inlet boundary condition was imposed on the external spherical boundary of the computational domain to prescribe the free-stream flow conditions. Four forward-flight velocity cases were investigated, corresponding to inlet velocities of 1 m/s, 10 m/s, 20 m/s, and 30 m/s. All helicopter surfaces, including the fuselage, fairing, tail and landing skids were modeled using wall boundary conditions. The numerical solution was obtained using the Coupled pressure–velocity algorithm, while second-order spatial discretization schemes were employed for all governing equations in order to improve solution accuracy and reduce numerical diffusion effects. Convergence was monitored through the evolution of the residuals and the stabilization of the aerodynamic loads. The solution was considered converged once the residuals reached a plateau region and the aerodynamic forces and moments acting on the helicopter configuration had variations less than 10^{-3} in order of magnitude over successive 500 iterations.

3. RESULTS

The aerodynamic behavior of both helicopter configurations was investigated for forward-flight velocities of 1 m/s, 10 m/s, 20 m/s, and 30 m/s. The numerical results highlight the influence of the aerodynamic fairing on the flow separation regions, wake development, and drag reduction.

The drag values obtained for the two configurations are summarized in Figure 4. The results show that the fairing significantly reduces the drag force for all investigated flight velocities. At low-speed flight conditions corresponding to hover-like operation, the drag decreases from 15 N to 10 N. As the flight velocity increases, the aerodynamic benefit of the fairing becomes more pronounced, with the drag reduction reaching approximately 48%.

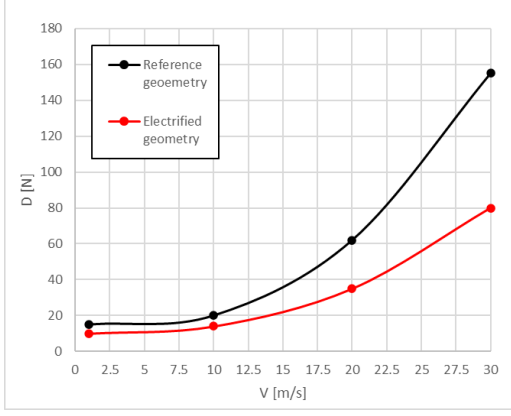

Figure 4. Drag variation with free stream velocity for reference and electrified geometry

The separated flow regions corresponding to each configuration are presented in Figure 5. For all investigated flight regimes, the addition of the aerodynamic fairing leads to a noticeable reduction of the separated flow areas. This behavior indicates an improvement in the flow attachment over the fuselage and tail boom regions, resulting in a reduction of the aerodynamic drag generated by the helicopter configuration. As the freestream velocity increases, the reference geometry shows a reduction of the separated flow region mainly around the tail area for all investigated velocities, while separation from the cabin region is observed only under hover-like conditions. In contrast, the electrified configuration presents significantly smaller separation regions. These regions decrease further as the freestream velocity increases and remain mainly confined to the aft part of the fairing, on both the upper and lower surfaces.

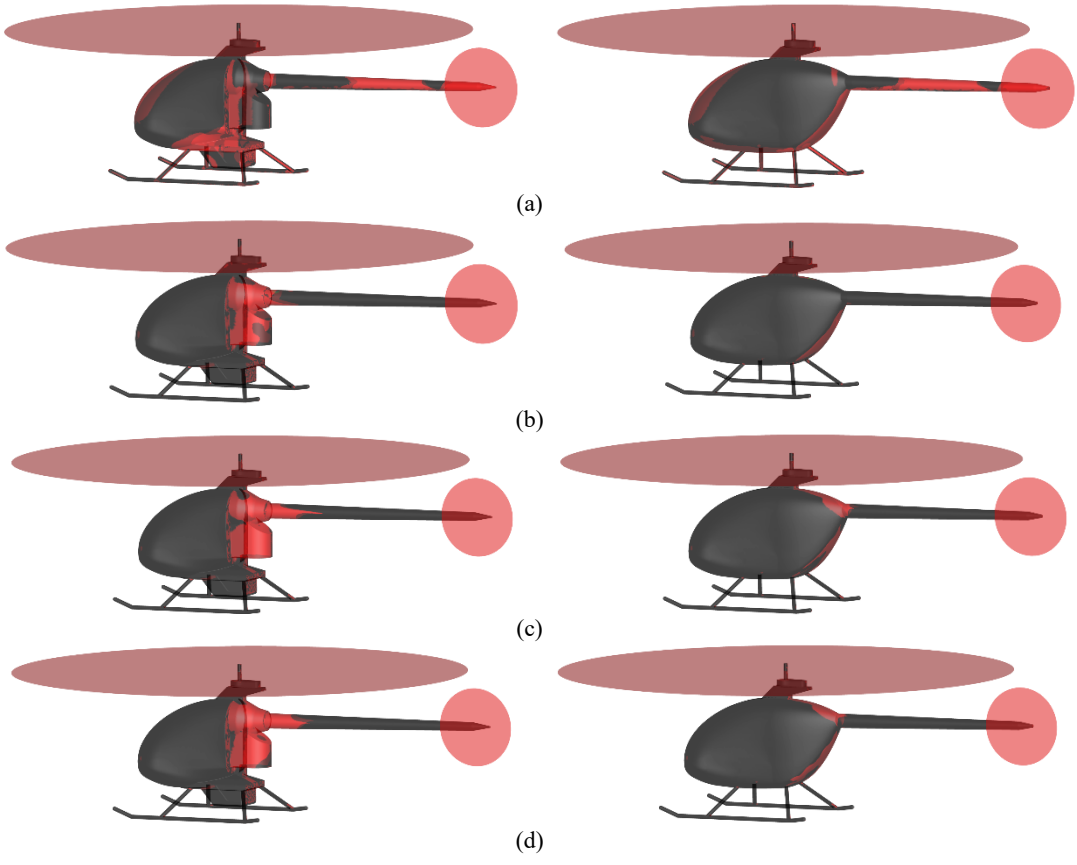

Figure 5. Separated flow region for both reference and electrified configurations at (a) V=1m/s, (b) V=10m/s, (c) V=20m/s, (d) V=30m/s

The surface skin-friction coefficient distributions presented in Figure 6 provide additional insight into the aerodynamic flow behavior around the helicopter geometry. The comparison between the two configurations shows that the fairing improves the flow attachment, particularly in the tail boom region.

For the case corresponding to $V = 30m/s$, higher skin-friction coefficient values are observed on the fairing surfaces and downstream fuselage regions, indicating a more energized attached boundary layer.

In contrast, near null skin-friction regions correspond to separated flow areas characterized by recirculation and reduced momentum exchange near the wall.

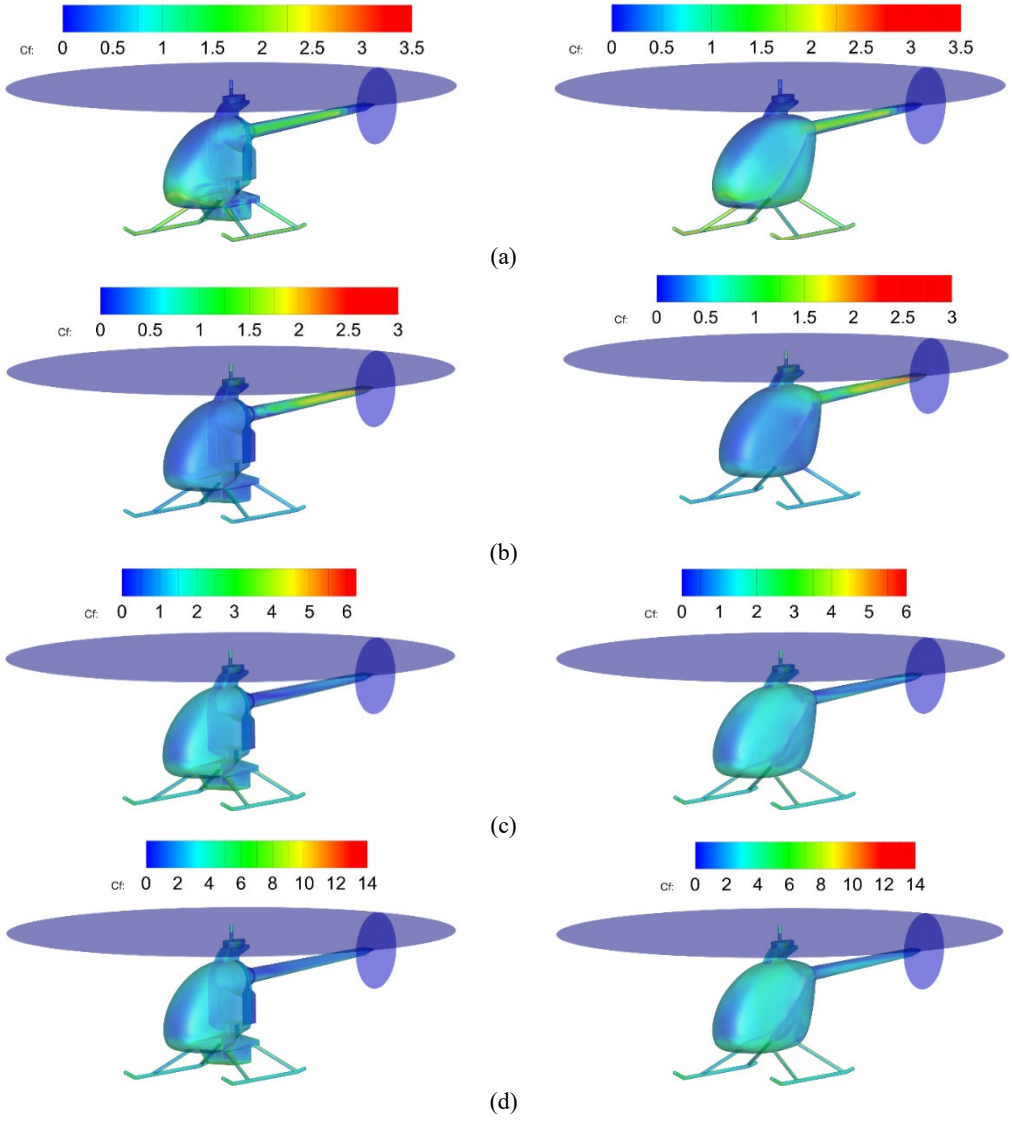

Figure 6. Skin friciton coefficient for both reference and electrified configurations at (a) V=1m/s, (b) V=10m/s, (c) V=20m/s, (d) V=30m/s

The streamline visualizations and velocity contours in the symmetry plane, shown in Figure 7, further emphasize the aerodynamic improvements introduced by the fairing integration.

In the hover condition $V = 1m/s$, the fairing contributes to a more uniform flow distribution around the fuselage and battery compartment.

For the higher forward-flight velocities $V = 10, 20,$ and $30\ m/s$, the integration of the battery pack within the fairing volume reduces the wake intensity and recirculation zones downstream of the fuselage, contributing to the observed drag reduction. The streamline representation also highlights the aerodynamic influence of the tail rotor and its interaction with the fuselage wake. The induced flow generated by the anti-torque rotor modifies the local velocity field near the tail boom and contributes to the overall wake structure of the helicopter configuration.

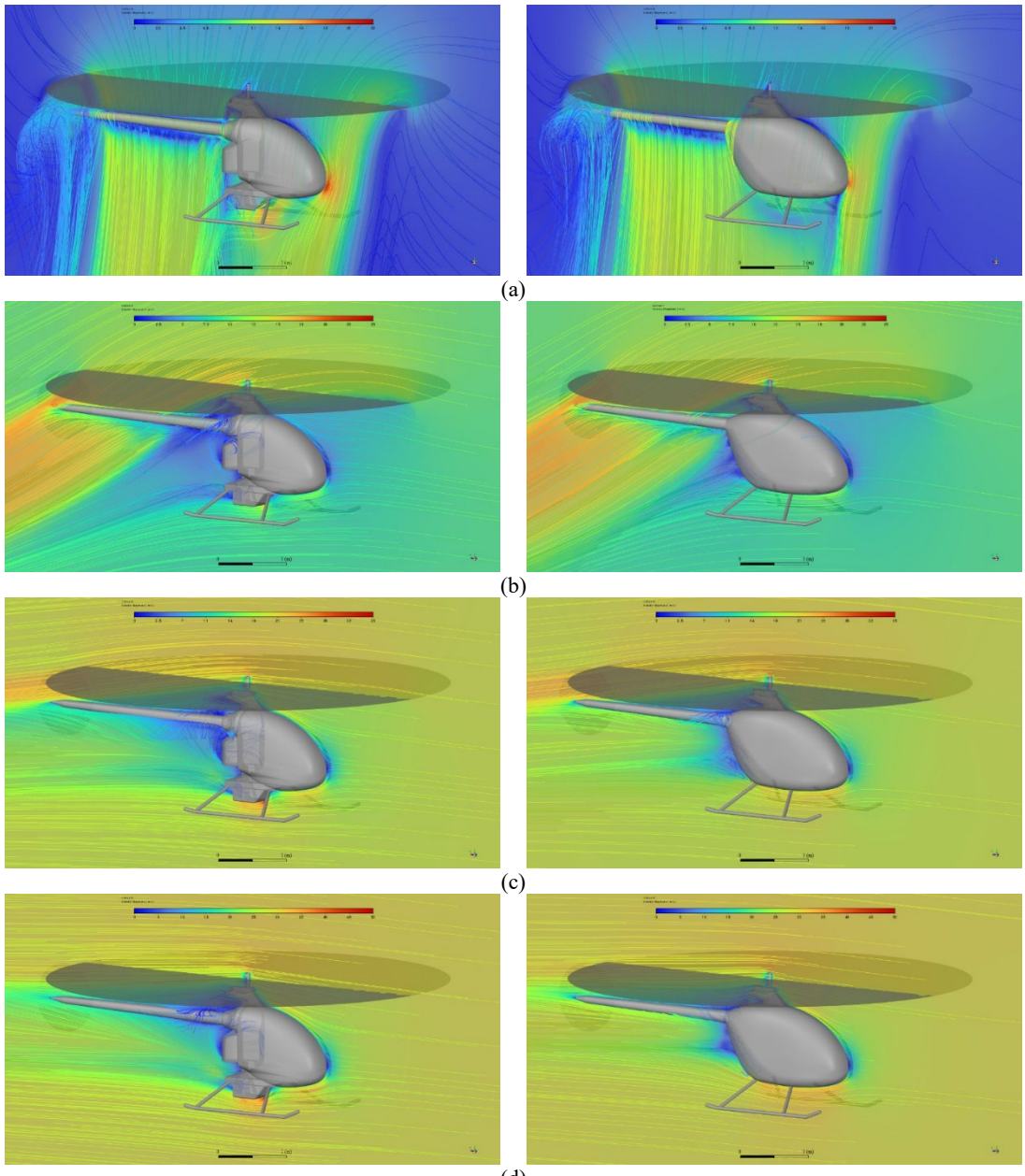

Figure 7. Streamline representation for both reference and electrified configurations at (a) V=1m/s, (b) V=10m/s, (c) V=20m/s, (d) V=30m/s

The helicopter performance calculations were conducted using a semi-empirical rotorcraft performance model based on the main geometric, aerodynamic, and propulsion characteristics of the investigated light helicopter configurations. The analysis considered a helicopter mass of 280 kg equipped with a two-bladed main rotor of radius 2.975 m and constant blade chord of 0.17 m operating at a rotational speed of 600 RPM. Standard atmospheric conditions at sea level were assumed as the reference state, with $\rho_0 = 1.225 kg/m^3$, while the maximum continuous available power was set to 48 kW. To account for realistic rotorcraft operating conditions, several correction coefficients associated with induced flow non-uniformity,

aerodynamic losses, and propulsion inefficiencies were incorporated into the model. The parasitic aerodynamic drag was estimated using the equivalent flat-plate area parameter. For the baseline helicopter configuration, a value of $f_A = 0.85m^2$ was considered, whereas the electrified configuration employed a reduced equivalent flat-plate area of $f_A = 0.425m^2$, reflecting the aerodynamic improvement associated with the integration of the optimized external fairing around the electric propulsion and battery systems. This reduction in equivalent drag area highlights the beneficial aerodynamic influence of the fairing on the overall fuselage flow organization and parasite drag reduction. Figure 8 illustrates the flight envelope corresponding to the two investigated configurations: the baseline helicopter geometry and the electrified configuration incorporating the external aerodynamic fairing. The curves represent the minimum flight velocity V_{min}, maximum flight velocity V_{max} and optimal operating velocity V_{opt} as functions of altitude. For both configurations, the admissible velocity range expands with increasing altitude, reflecting the variation of aerodynamic and rotor performance characteristics under changing atmospheric conditions. The electrified configuration shows a noticeable shift of the upper velocity boundary toward higher values, particularly at medium and high altitudes, indicating an enhancement in forward-flight aerodynamic performance compared to the reference geometry. The evolution of the optimal velocity curve demonstrates that V_{opt} increases progressively with altitude for both cases. However, the electrified configuration achieves consistently higher optimal operating speeds. This behavior can be attributed to the beneficial aerodynamic effect of the external fairing, which improves flow around the fuselage. Furthermore, the wider separation between V_{min} and V_{max} observed for the electrified configuration suggests an enlarged operational flight envelope and improved mission flexibility. These results confirm that the aerodynamic integration of the electrification system through an optimized fairing contributes positively to the overall aerodynamic efficiency of the helicopter, especially in medium- and high-speed forward-flight regimes.

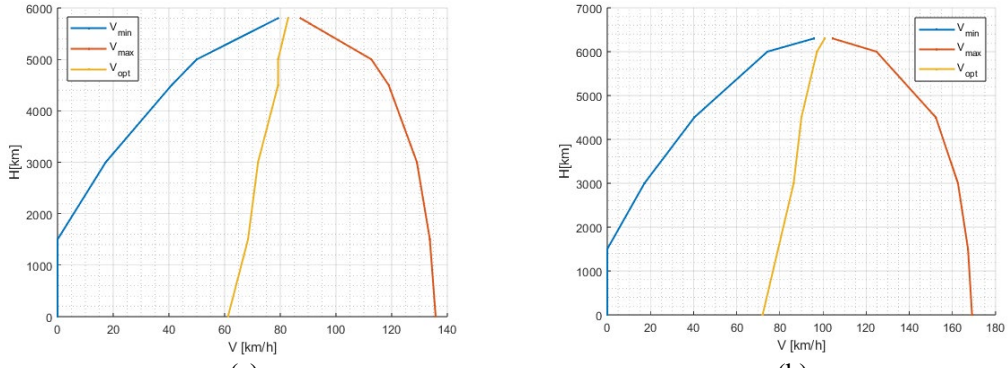

Figure 8. Flight envelope for (a) reference geometry and (b) electrified configuration

Figure 9 presents the power required P_R and available power P_A distributions as functions of forward-flight velocity for different operating altitudes, corresponding to the baseline configuration and the electrified configuration. The solid curves denote the required power, while the dashed horizontal lines represent the available power at each altitude. For both configurations, the required power curves present the characteristic U-shaped behavior associated with rotary-wing aircraft performance. At low forward-flight velocities, the power demand is relatively high due to induced power losses in hover and near-hover conditions. As the velocity increases, the required power decreases, reaching a minimum in the medium-

speed regime where the aerodynamic efficiency is maximized. Beyond this operating region, the required power rises rapidly as parasite drag and compressibility effects become increasingly dominant. A progressive reduction in available power with increasing altitude is observed for both configurations, reflecting the degradation in propulsion and aerodynamic performance caused by decreasing air density. Simultaneously, the required power curves shift upward at higher altitudes, reducing the margin between P_R and P_A, and consequently limiting the achievable maximum flight velocity. Compared to the baseline geometry, the electrified configuration demonstrates consistently lower required power values over a broad range of forward-flight speeds, particularly in the medium and high-speed regimes. In addition, the minimum of the required power curve for the electrified configuration occurs at slightly higher velocities, suggesting a shift of the optimal cruise condition toward faster forward-flight operation. The gradient of the required power at high velocities further confirms the beneficial aerodynamic influence of the fairing on wake development and fuselage-flow interaction. Overall, the results demonstrate that the aerodynamic integration of the electrification architecture positively affects helicopter performance across a wide range of flight conditions and altitudes.

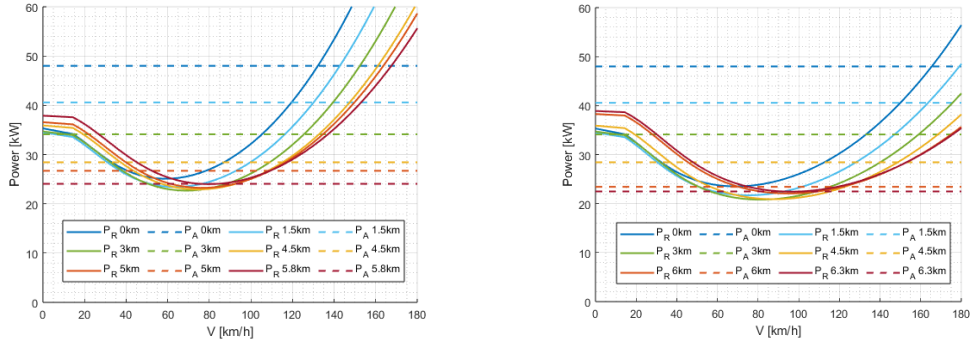

(a) (b)

Figure 9. Available power and required power for (a) reference and (b) electrified geometry with respect to forward velocity at different altitudes

Figure 10 illustrates the variation of vertical climb velocity V_z as a function of forward-flight velocity for different operating altitudes, corresponding to the baseline helicopter geometry (a) and the electrified configuration (b). The results provide insight into the climb performance characteristics and the influence of the aerodynamic fairing integrated within the electrified architecture.

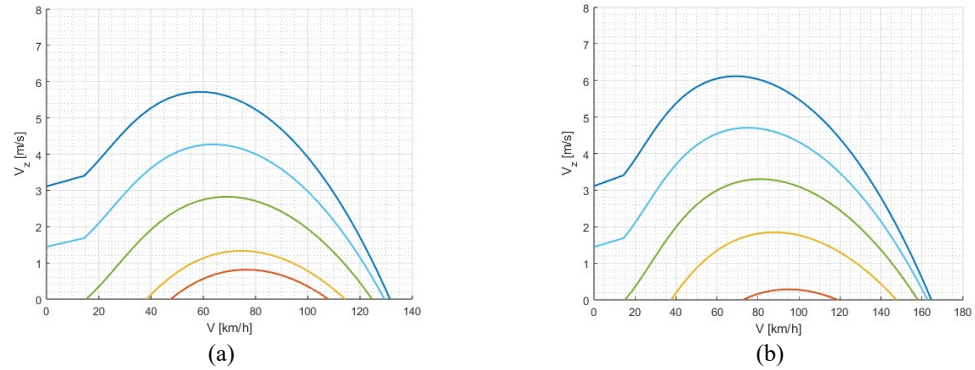

(a) (b)

Figure 10. Vertical velocity variation of the (a) reference geometry and (b) electrified configuration with respect to forward velocity at different altitudes

For both configurations, the vertical velocity profiles present a bell-shaped evolution with increasing forward-flight velocity. At low forward speeds, the climb capability remains limited due to high induced power losses associated with rotor operation in near-hover conditions. As the forward velocity increases, the rotor aerodynamic efficiency improves, leading to a progressive increase in climb rate until a maximum value is reached in the medium-speed flight regime. Beyond this optimum region, the vertical velocity decreases as parasite drag and power requirements rise significantly at higher forward-flight speeds. The effect of altitude is clearly visible in both cases. Increasing altitude leads to a systematic reduction in maximum climb performance due to the decrease in air density, which negatively affects rotor thrust generation and available propulsion power. Consequently, the peak values of V_z become progressively lower at higher altitudes, while the operational velocity interval associated with positive climb performance is reduced. Compared to the baseline configuration, the electrified configuration demonstrates consistently improved climb performance across the investigated velocity range. The maximum vertical velocities are higher, and the curves extend toward larger forward-flight velocities before reaching the zero-climb condition. This behavior indicates that the aerodynamic fairing surrounding the electrification components contributes to a reduction in aerodynamic drag and improves the overall flow organization around the fuselage. Furthermore, the electrified configuration maintains positive climb capability over a broader operational envelope, particularly at medium and high forward-flight speeds.

4. CONCLUSIONS

The present study investigated the aerodynamic influence of integrating an external fairing for helicopter electrification using high-fidelity CFD simulations. Two helicopter configurations were analyzed: a baseline geometry and a modified electrified configuration incorporating battery modules, electric propulsion components, and an external aerodynamic fairing. The aerodynamic behavior of both configurations was evaluated for multiple forward-flight conditions ranging from hover-like operation to moderate forward-flight velocities.

The numerical simulations demonstrated that the addition of the aerodynamic fairing significantly improves the external flow behavior around the helicopter fuselage. The modified configuration exhibited substantially smaller flow separation regions compared to the baseline geometry for all investigated freestream velocities. The drag analysis revealed a considerable reduction in aerodynamic drag for the electrified configuration. At hover conditions, the drag decreased from 15 N to 10 N, while at the maximum investigated flight velocity of 30 m/s, the drag reduction reached approximately 48%. These improvements are directly associated with the reduction of separated flow regions and the smoother aerodynamic transition provided by the fairing integration. The skin-friction coefficient distributions and streamline visualizations further confirmed the beneficial aerodynamic effects of the fairing. The modified configuration demonstrated reduced recirculation zones downstream of the fuselage and tail.

The flight performance analysis indicated that the aerodynamic improvements obtained through fairing integration also contribute to enhanced climb performance. The modified configuration exhibited increased maximum vertical velocity and improved aerodynamic efficiency, with the optimal climb regime shifted toward higher forward-flight velocities. However, the simulations also showed the expected degradation of climb capability with increasing altitude due to the reduction in atmospheric density and available excess power.

Overall, the obtained results demonstrate that the aerodynamic integration of electrification components using optimized external fairings can significantly improve the aerodynamic efficiency and flight performance of light helicopter configurations.

ACKNOWLEDGMENTS

The authors acknowledge the financial support provided through the project "Sistem inovativ de stocare a energiei pentru aplicații hibride și electrice în industria aeronautică și automobilistică" (SMIS Code: 121806), funded under the "Programul Operațional Competitivitate", Call POC/163/1/3 – "Stimularea cererii întreprinderilor pentru inovare prin proiecte CDI derulate de întreprinderi individual sau în parteneriat cu institute de CD şi universități, în scopul inovării de procese și de produse în sectoarele economice care prezintă potențial de creștere."

The authors would also like to acknowledge the collaboration and technical support of ATNOM SRL, as project leader, and National Institute for Aerospace Research "Elie Carafoli", as project partner, for their valuable contributions to the research and development activities carried out within this project.

REFERENCES

[1] M. Hepperle, *Electric Flight – Potential and Limitations*, Deutsches Zentrum für Luft- und Raumfahrt (DLR), 2012.
[2] C. Pornet, and A. T. Isikveren, Conceptual Design of Hybrid-Electric Transport Aircraft, *Progress in Aerospace Sciences*, Vol. **79**, 2015, pp. 114–135.
[3] C. Friedrich, and P. A. Robertson, Hybrid-Electric Propulsion for Aircraft, *Journal of Aircraft*, Vol. **52**, No. 1, 2015, pp. 176–189.
[4] J. G. Leishman, *Principles of Helicopter Aerodynamics*, Cambridge University Press, Cambridge, UK, 2006.
[5] W. Johnson, *Rotorcraft Aeromechanics*, Cambridge University Press, Cambridge, UK, 2013.
[6] S. Sahoo, X. Zhao, and K. Kyprianidis, A Review of Concepts, Benefits, and Challenges for Future Electrical Propulsion-Based Aircraft, *Aerospace*, Vol. **7**, No. 4, 2020.
[7] S. F. Hoerner, *Fluid-Dynamic Drag*, Hoerner Fluid Dynamics, 1965.
[8] P. R. Spalart, Strategies for Turbulence Modelling and Simulations, *International Journal of Heat and Fluid Flow*, Vol. **21**, No. 3, 2000, pp. 252–263.
[9] F. R. Menter, Two-Equation Eddy-Viscosity Turbulence Models for Engineering Applications, *AIAA Journal*, Vol. **32**, No. 8, 1994, pp. 1598–1605.
[10] R. G. Rajagopalan, RotCFD – A Tool for Aerodynamic Interference of Rotors, *American Helicopter Society Future Vertical Lift Aircraft Design Conference*, 2012.
[11] W. Johnson, *NDARC — NASA Design and Analysis of Rotorcraft*, NASA Technical Report, 2015.
[12] M. Biava, W. Khier, and L. Vigevano, CFD Prediction of Air Flow Past a Full Helicopter Configuration, *Aerospace Science and Technology*, Vol. **15**, No. 6, 2011, pp. 437–451.
[13] N. K. Madavan, *Thermal Management in Electrified Aircraft Propulsion Systems*, NASA Technical Publications, 2018.
[14] C. Silva, W. Johnson, E. Solis, and M. Patterson, *VTOL Urban Air Mobility Concept Vehicles for Technology Development*, NASA Technical Memorandum, 2018.
[15] B. J. Brelje, and J. R. R. A. Martins, Electric, Hybrid, and Turboelectric Fixed-Wing Aircraft: A Review of Concepts, Models, and Design Approaches, *Progress in Aerospace Sciences*, Vol. **104**, 2019, pp. 1–19.